Journal of Solid State Chemistry 184 (2011) 455–462

Contents lists available at ScienceDirect

Journal of Solid State Chemistry

journal homepage: www.elsevier.com/locate/jssc

Novel pseudo-morphotactic synthesis and characterization of tungsten nitride nanoplates

Deliang Chen [a,b,*], Hejing Wen [a], Tao Li [a], Li Yin [a], Bingbing Fan [a], Hailong Wang [a], Rui Zhang [a,c], Xinjian Li [b], Hongliang Xu [a], Hongxia Lu [a], Daoyuan Yang [a], Jing Sun [d], Lian Gao [d]

[a] School of Materials Science and Engineering, Zhengzhou University, 100 Science Road, Zhengzhou 450001, China
[b] School of Physics and Engineering, Zhengzhou University, 100 Science Road, Zhengzhou 450001, China
[c] Laboratory of Aeronautical Composites, Zhengzhou Institute of Aeronautical Industry Management, Zhengzhou 450046, China
[d] The State Key Laboratory of High Performance Ceramics and Superfine Microstructure, Shanghai Institute of Ceramics, Chinese Academy of Sciences, 1295 Dingxi Road, Shanghai 200050, China

ARTICLE INFO

Article history:
Received 30 September 2010
Received in revised form
8 December 2010
Accepted 18 December 2010
Available online 28 December 2010

Keywords:
Tungsten nitride nanoplate
Tungstate-based hybrid
Morphology
Crystal growth
Morphotactic transformation

ABSTRACT

A novel pseudo-morphotactic transformation route was developed to synthesize polycrystalline β-W_2N nanoplates by thermally treating tungstate-based inorganic–organic hybrid nanobelts with a lamellar microstructure in an NH_3 flow. The tungstate-based hybrid nanobelts were formed in a water-in-oil-microemulsion-like "commercial H_2WO_4 powders/*n*-octylamine/heptane" reaction system. The as-obtained hybrid nanobelts were thermally treated in an NH_3 atmosphere at 650–800 °C for 2 h to form cubic β-W_2N nanoplates. XRD, SEM, TEM, FT-IR and TG-DTA were used to characterize the precursors and their final products. The polycrystalline β-W_2N nanoplates derived from hybrid nanobelts, with side lengths of several hundred nanometers, consist of small nanocrystals with an average grain size of 3.2 nm. The formation of β-W_2N nanoplates involved two steps: decomposing tungstate-based hybrid nanobelts into WO_y and W species and then nitridizing the active W-containing species to β-W_2N nanocrystals in an NH_3 flow. The platelike morphology of the β-W_2N nanocrystals was inherited from the precursor of tungstate-based inorganic–organic hybrid nanobelts.

1. Introduction

Nitrides (or carbonitrides) of transition metals have attracted increasing attention due to their profuse scientific aspects and wide industrial applications [1–3]. Recently TiN [4], CrN [5], GaN [6] and ZrN [7] have been intensively investigated in synthetic methods, structural characterization and applications. As one important member of metal nitrides, tungsten nitrides (W_xN) have many promising properties, including good chemical stability, high strength, high hardness, high melting point with good electrical conductivity and a relative low band gap (2.2 eV) [8–10]. These unique properties make tungsten nitrides and related tungsten-containing ternary nitrides have wide applications in the following aspects: effective barriers against diffusion of copper in microelectronic circuits [11–13], gate electrodes in MOS devices [14], Schottky contacts on AlGaN/GaN heterostructures [15], contact barrier for DRAM [16], wear-resistant coatings [10], contamination resistant coatings [17], photocatalysts for water decomposition using solar light [9], cathode catalysts for fuel cells [18] and catalysts for NO dissociation [19].

In the W–N system, there are two main phases in the region of $N/W \leq 1$, i.e., tungsten mononitride WN and tungsten subnitride β-W_2N [20]. For the tungsten mononitride WN, there are two structural modifications of low temperature hexagonal h-WN and high temperature cubic c-WN [20]. The calculated results on the basis of the first-principles method indicate that WN has eight different crystal structures and the NiAs-type WN is the most energy favorable and ultra-incompressible, and the WC-type WN is metastable [21].

Tungsten nitride and carbonitride films are the major using form in electronic devices and protective coatings. Atomic layer deposition (ALD) method is one of the most efficient routes to fabricate WN_xC_y films [22,23] and WN_x films [20,24,25] on various surfaces, due to its ability of precise control of film thicknesses [13]. Chemical vapor deposition (CVD) [11], metal–organic CVD (MOCVD) method [26,27], and plasma-enhanced chemical vapor deposition [28] are frequently used to synthesize WN_xC_y, $WN_{1.5}O_{0.1}$ and WN_x thin films. DC reactive magnetron sputtering [29], reactive r.f. magnetron sputtering [14,30], and ion-beam assisted deposition are also developed to fabricate CrWN, CrN/WN and WN_x films [31].

* Corresponding author at: School of Materials Science and Engineering, Zhengzhou University, 100 Science Road, Zhengzhou 450001, China.
E-mail addresses: dlchen@zzu.edu.cn, dlchennano@hotmail.com (D. Chen).

0022-4596/$ - see front matter © 2010 Elsevier Inc. All rights reserved.
doi:10.1016/j.jssc.2010.12.018

Tungsten nitrides and their related micro-/nanocrystals are usually synthesized by thermal treating tungsten containing precursors under an ammonia atmosphere [2,19,25], and the precursors are usually formed from soluble reagents, such as tungsten hexachloride [2,3,32], and bis(*tert*-butylimido)bis-(dimethylamido)-tungsten(IV) [33]. Cubic β-W_2N nanoparticles with sizes of 2–3 nm were first synthesized by thermolysis of $W(N^tBu)_2(Ph_2pz)_2$ at 800 °C under a nitrogen condition [34]. Ma and coworkers [8] reported a synthesis of β-W_2N nanoparticles (5–40 nm) with a direct-current arc discharge method using W and nitrogen as starting materials. Rugge and coworkers [35] synthesized β-W_2N inverse opal structures by infiltrating thin-film silica colloidal crystals using an ALD method using bis(*tert*-butylimido)bis-(dimethylamido) tungsten(IV) and ammonia as the starting materials. Lei and coworkers [36] synthesized hexagonal WN nanoparticles with a size of 5 nm by thermally treating the pellets of ammonium dicyanamide and WO_3 in a vacuum silica ampoule at 850 °C. Bai and coworkers [37] synthesized mesostructural β-W_2N nanocrystals with a high surface area (89 m^2/g) via a temperature-programmed reaction of H_2WO_4 with ammonia at 700 °C. Although there are several methods developed for the successful synthesis of tungsten nitride nanocrystals, the facile, inexpensive and efficient routes for the shape- and size-controlled synthesis are not still available [3,19,34].

Recently we proposed a general route to fabricate mesostructural tungstate-based inorganic–organic hybrid nanobelts with highly ordered lamellar microstructures using $H_2W_2O_7 \cdot xH_2O$ and *n*-alkylamines as the starting materials [38–40]. The above tungstate-based inorganic–organic hybrid nanobelts were found to be an excellent precursor for the synthesis of WO_3 nanoplates and WO_3 nanoparticles with superhigh specific surface areas and enhanced gas-sensing properties [41–44]. The advantage of the precursor routes towards inorganic nanocrystals is the controllability in shapes and sizes of the products.

In this work, we extend the precursor method to synthesize tungsten nitride nanocrystals with controlled morphology using commercial H_2WO_4 powders as the tungsten source for the first time. The synthetic process includes two steps: (1) H_2WO_4 powders firstly react with *n*-octylamine to form one-dimensional tungstate-based inorganic–organic hybrid nanobelts. (2) The as-obtained hybrid nanobelts are then thermally treated in an NH_3 flow to fabricate tungsten nitride nanoplates. The transformation from commercial H_2WO_4 powders to polycrystalline β-W_2N nanoplates via tungstate-based inorganic–organic hybrid nanobelts can be schematically shown in Fig. 1. The objective of the work is to verify the possibility to transform the plate-like shape of the hybrid precursor to the final product of tungsten nitride nanocrystals. The phase compositions, microstructures and formation mechanisms of the precursors and final products are investigated. The essential novelty of this work is the morphology-controlled synthesis of β-W_2N nanoplates using commercial H_2WO_4 powders as starting materials by a pseudo-morphotactic transformation route via tungstate-based inorganic–organic hybrid nanobelts with highly ordered lamellar structures.

2. Experimental section

2.1. Synthesis of tungstate-based inorganic–organic hybrid nanobelts

The tungstate-based inorganic–organic hybrids were synthesized by a reaction between H_2WO_4 and *n*-octylamine in heptane. Typically 10 g of H_2WO_4 powders (Sinopharm Chemical Reagent Co., Ltd., AR) was dispersed in a mixture of 0.4 mol of *n*-octylamine (Sinopharm Chemical Reagent Beijing Co., Ltd., CP) and 530 ml of heptane (Tianjin Huadong Reagent Factory, AR) under a constant magnetic stirring at room temperature for 24 h. The molar ratio of *n*-octylamine to H_2WO_4 was 10:1 and the volume ratio of heptane to *n*-octylamine was 8:1. After another reaction time of 48 h, the resultant white solids were collected by centrifugation, washed with ethanol, and then dried under a reduced pressure at room temperature for 48 h. The dried sample was tungstate-based inorganic–organic hybrid nanobelts, which were used as the precursor for synthesis of tungsten nitride nanoplates.

2.2. Synthesis of tungsten nitride nanoplates from tungsten-based hybrid nanobelts

Typically 0.5 g of tungstate-based inorganic–organic hybrid nanobelts was placed in a semi-cylindrical alumina crucible, and the crucible was then inserted to the center of a tubular quartz furnace (ø500 mm × 1000 mm) in a lying manner. The hybrid sample should be uniformly placed along the crucible wall, and the end with a baffler was towards the gas-down direction. The gas-out end of the quartz tube was loosely stuffed with a porous cylindrical alumina tile. The quartz tube was first purged with a high-pure Ar gas (100 ml/min) for 1 h to discharge the air. After the Ar gas was closed and the NH_3 gas was simultaneously opened with a flux of 80 ml/min, the furnace was rapidly heated to 500 °C with a heating rate of 25 °C/min, and then slowly heated from 500 to 650–800 °C with a heating rate of 2 °C/min. After kept at 650–800 °C for 2 h, the furnace naturally cooled down to room temperature under an NH_3-gas condition. The collected solid powders were tungsten nitride nanoplates with a mass of 0.15–0.17 g.

For the purpose of comparison, commercial H_2WO_4 powders were used as the tungsten source to synthesize tungsten nitride under a similar condition. Typically 0.79 g of H_2WO_4 powders was placed in the semi-cylindrical alumina crucible, which was then inserted into the tubular quartz furnace. The quartz tube was purged with a high-pure Ar gas (100 ml/min) for 1 h, before the NH_3 gas with a flux of 80 ml/min was opened. The furnace was heated to 500 °C at a rate of 25 °C/min, and then to 750 °C at a heating rate of 2 °C/min. The sample was kept at 750 °C for 2 h under a continuous NH_3 flow.

2.3. Characterization and analysis

The phase compositions were identified by X-ray diffraction (XRD) equipment (ZHJ XPERT PRO, China) with a Cu$K\alpha$ radiation

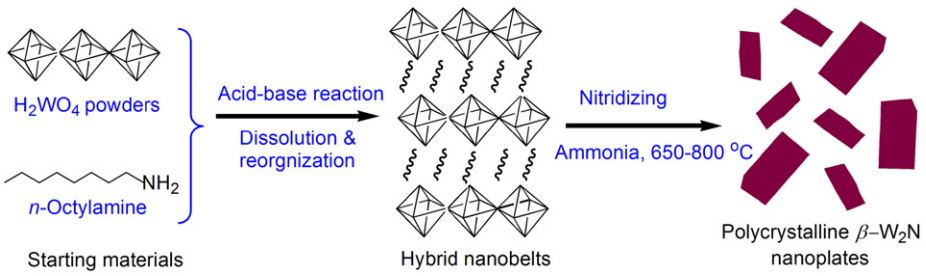

Fig. 1. A schematic of the pseudo-morphotactic route for the synthesis of polycrystalline β-W_2N nanoplates from commercial H_2WO_4 powders.

(λ=1.5406 Å) and a graphite monochrome under a voltage of 36 kV and a current of 20 mA. The XRD patterns were recorded with a speed of 2°/min. The morphologies were observed on a scanning electron microscope (SEM, FEI QUANTA-200, Holland), and on a transmission electron microscope (TEM, JEOL JEM-2100F, Japan). TG-DTA curves were recorded on a thermal analysis system (NETZSCH STA409PC, Germany) with a heating rate of 5 °C/min in an air flow. Fourier-transform infrared spectra (FT-IR, Nicolet460) were applied to characterize the hybrid precursor using the KBr disk technique in room temperature. The KBr was not dried before use.

3. Results

3.1. Structures and morphology of tungstate-based hybrids

Fig. 2 shows the XRD pattern of the product derived from the reaction of commercial H_2WO_4 powders with *n*-octylamine in heptane. There are seven intense diffraction peaks at 2.41°, 5.82°, 9.21°, 12.64°, 16.03°, 19.49° and 22.94° with gradually decreasing intensities. When compared the product and its starting material of H_2WO_4 (the inset of Fig. 2), one can find that the diffraction peaks belonging to orthorhombic H_2WO_4 (JCPDS card no. 43-0679) in a 2θ range of 15–60° disappear, and the as-obtained product just shows diffraction peaks in the low-2θ range of 1–25° (Fig. 2a). These results indicate that the as-obtained product is of a completely new structure, i.e., an ordered lamellar structure, according to the previously reported data [38]. The diffraction peaks at the low-2θ range can be indexed to (00*l*) reflections, and l=1, 2, 3, 4, 5, 6 and 7 for 2.41°, 5.82°, 9.21°, 12.64°, 16.03°, 19.49° and 22.94°, respectively. The high intensities and the large number of the diffraction peaks suggest the as-obtained hybrid product is of a highly ordered lamellar structure. The interlayer distance (d) can be calculated to be 2.76(3) nm according to the (00*l*) reflections by minimizing the sum of squares of the residuals in 2θ values [38].

The morphology of the hybrid product derived from a reaction of commercial H_2WO_4 powders with *n*-octylamine in heptane is shown in Fig. 3. A low-magnification SEM image (Fig. 3a) shows the as-obtained product consists of fibriform structures in a large view-field. The enlarged SEM image (Fig. 3b) suggests that the fibriform product is of one-dimensional structures with lengths of

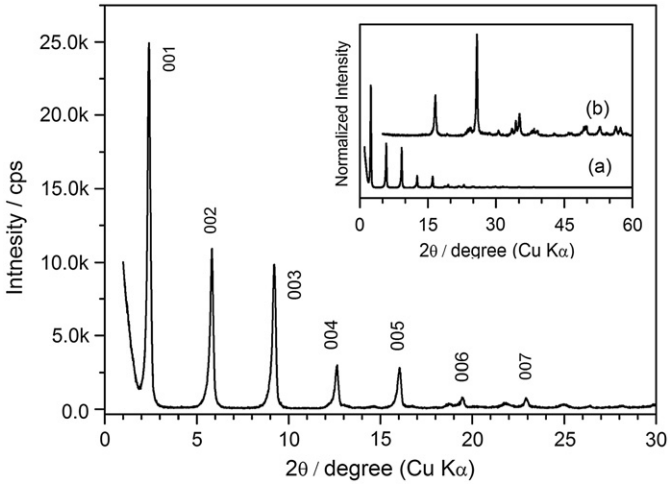

Fig. 2. The XRD pattern of the tungstate-based inorganic–organic hybrid nanobelts derived from commercial H_2WO_4 and *n*-octylamine in heptane. The inset is the large 2θ-range XRD patterns of (a) the hybrid and (b) the corresponding starting material of H_2WO_4 powders.

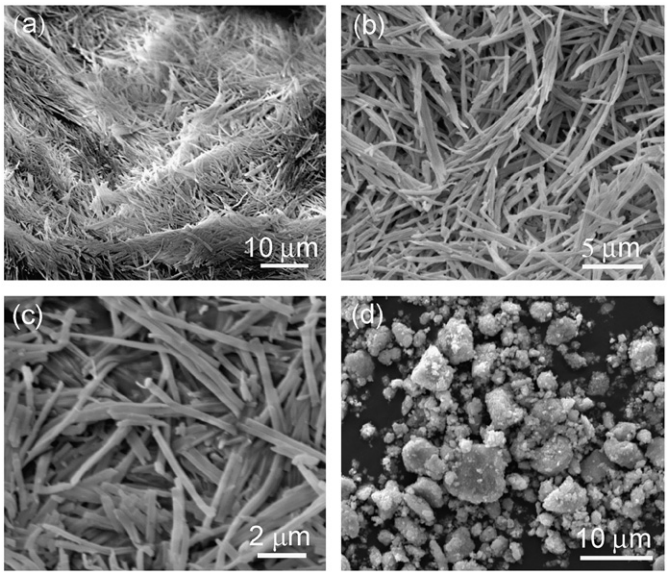

Fig. 3. SEM images of (a–c) the tungstate-based inorganic–organic hybrid nanobelts and (d) the corresponding starting material of H_2WO_4 powders.

5–20 μm. Fig. 3c shows a high-magnification image, which indicates that the one-dimensional structures are uniform nanobelts with apparent widths of 100–300 nm, and their length-to-width ratios are larger than 50. Fig. 3d shows a typical SEM image of H_2WO_4 powders used as a starting material. As Fig. 3d shows, the H_2WO_4 powders consist of irregular aggregates with a large particle-size distribution of 1–10 μm, and the small particles mostly consist of nanoparticles. From Fig. 3, one can find that the as-obtained hybrid product is completely different from its solid starting material in shapes and sizes, which suggests that a reorganization process has occurred during the formation of the one-dimensional product [38].

The typical FT-IR spectra of (a) the as-obtained product and (b) its starting material of H_2WO_4 powders are shown in Fig. 4. For H_2WO_4 (Fig. 4b), the intense and wide absorption band at round 693 cm^{-1} corresponds to the ν(O–W–O) stretching mode, and the absorption band at 941 cm^{-1} is assignable to the stretching mode of terminal W=O [38,45]. The absorption bands at 3418 and 1628 cm^{-1} correspond to the ν(O–H) stretching and the δ(O–H) bending modes of the adsorbed water molecules, respectively. For the as-obtained product, as shown as Fig. 4a, the ν(O–W–O) stretching mode is split to be two intense and sharp absorption bands. The absorption bands at 874 and 920 cm^{-1} are assignable to the stretching modes of terminal W=O [38,45]. The band at around 3210 cm^{-1} can be assigned to the stretching vibration of the N–H group. The bands at 1635 and 1582 cm^{-1} correspond to the δ(N–H) scissoring mode of the $-NH_2$ groups and the δ(N–H) bending mode of the $-NH_3^+$ groups, respectively [45]. The weak bands at 2510–2750 cm^{-1} can correspond to the symmetrical stretching bands of the $-NH_3^+$ groups [38]. The bands in the region of 2800–3000 cm^{-1} are assigned to the C–H stretching modes of the polymethylene ($-(CH_2)_n-$) chains (2850 cm^{-1}, $\nu_s(CH_2)$; 2917 cm^{-1}, $\nu_{as}(CH_2)$) and end-methyl ($-CH_3$) groups (2958 cm^{-1}, $\nu_{as}(CH_3)$) [38]. The band at 3432 cm^{-1} is assigned to the ν(O–H) stretching mode of adsorbed water molecules. A broad band appearing at around 2042 cm^{-1} is due to a combination of the asymmetrical bending vibration and torsional oscillation of the $-NH_3^+$ groups interacting with the apical oxygen of the W–O framework, i.e., R-$NH_3^+ \cdots {}^-$O–W [38,45], whereas no bands occur at this wavenumber range for H_2WO_4, as shown as Fig. 4. It should be noted that the peaks at 1401 and 3160 cm^{-1} are the

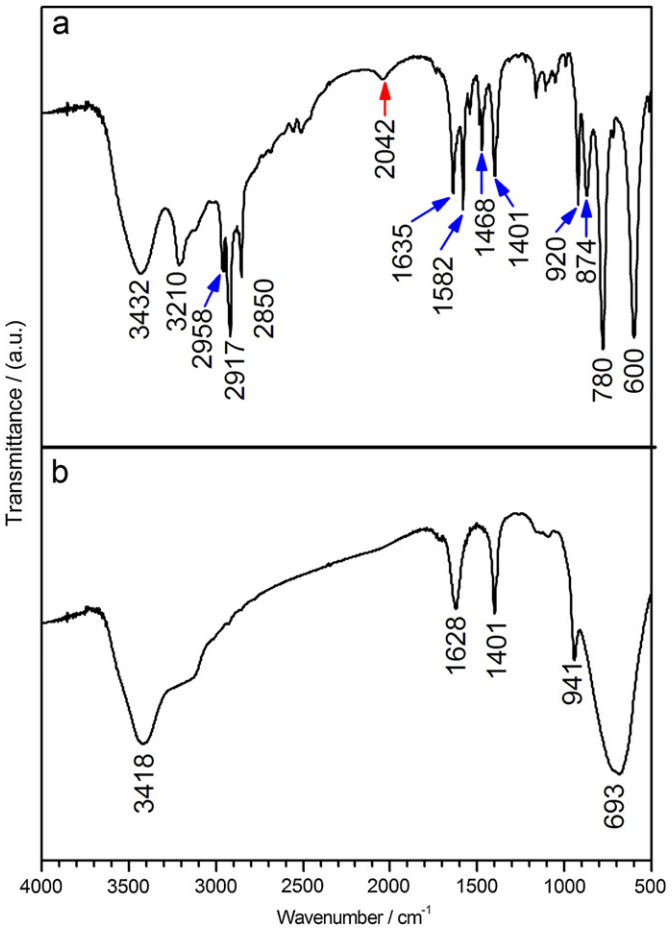

Fig. 4. FT-IR spectra of (a) the tungstate-based inorganic–organic hybrid nanobelts and (b) the corresponding H_2WO_4 powders.

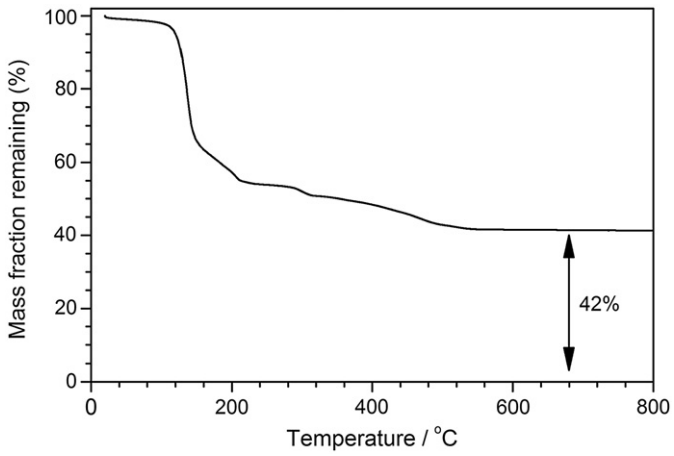

Fig. 5. A typical TG curve of the tungstate-based inorganic–organic hybrid nanobelts derived from commercial H_2WO_4 and *n*-octylamine in heptane.

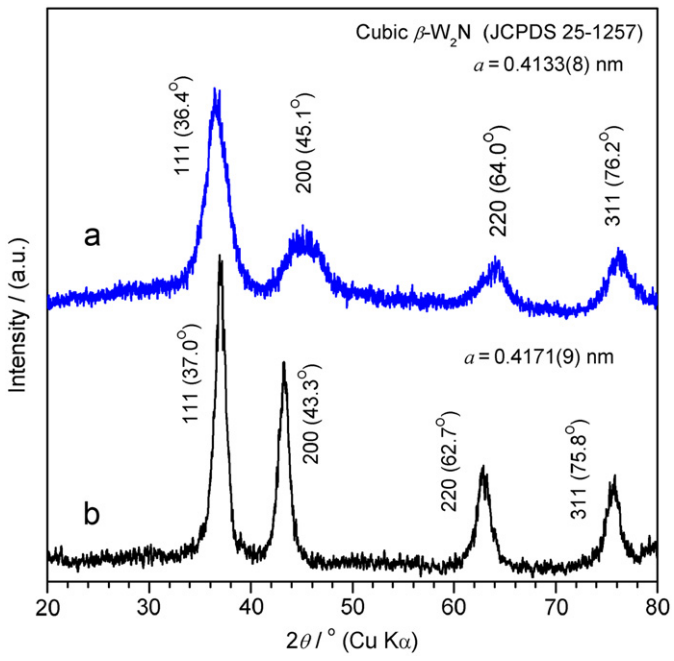

Fig. 6. Typical XRD patterns of (a) cubic β-W_2N nanoplates derived from the tungstate-based inorganic–organic hybrid nanobelts and (b) cubic β-W_2N nanocrystals derived from commercial H_2WO_4 powders.

background absorption bands from KBr without drying before use. The FT-IR results indicate that the as-obtained product from the reaction of H_2WO_4 and *n*-octylamine is composed of organic ammonium species and inorganic W–O layers [38].

Fig. 5 shows a typical TG curve of the as-obtained hybrid product from the reaction of H_2WO_4 and *n*-octylamine. There is a 58% mass loss during the temperature range 100–600 °C, and the mass fraction remaining should be the amount of WO_3 after treating at higher than 600 °C. The mass loss corresponds to the desorption of *n*-octylamine molecules, the decomposition of the organic species and the removal of the structural water of the inorganic W–O layers. When the XRD, SEM, FT-IR and TG results are taken into account, it can therefore be concluded that the product obtained from the reaction of H_2WO_4 and *n*-octylamine is composed of inorganic–organic hybrid nanobelts with an ordered lamellar structure, in which the inorganic W–O layers and the organic species are stacked alternately. According to the TG data and the previous reported results, the possible composition of the tungstate-based inorganic–organic hybrid nanobelts can be estimated to be $(C_8H_{17}NH_3)_2WO_4$ [38].

3.2. Phase and morphology of tungsten nitride nanoplates from tungstate-based hybrid nanobelts

A typical XRD pattern of the sample obtained by treating tungstate-based inorganic–organic hybrid nanobelts at 750 °C for 2 h in an NH_3 flow is shown in Fig. 6a. There are four obvious diffraction peaks at 36.4°, 45.1°, 64.0° and 76.2°, which can readily be indexed to the reflections from (111), (200), (220) and (311) planes of the cubic β-W_2N phase, respectively, according to the literature data (JCPDS card no. 25-1257; space group: *Pm*3*m* (221), a=0.4126 nm). The calculated cell parameters according to the XRD data and the minimum square method are $a=b=c=0.4133(8)$ nm, close to the literature data (a=0.4126 nm). As Fig. 6a shows, the diffraction peaks are obviously broadened, indicating that the product consists of nanocrystals with very small crystal sizes. According to the Debye–Scherrer equation ($d=0.89\lambda/B\cos\theta$), λ=0.15406 nm, $B\cos\theta$=0.0428 for the (111) reflection, and the calculated average size of the crystalline β-W_2N grains is about 3.2 nm.

Fig. 7 shows the typical SEM images of the as-obtained β-W_2N nanocrystals. The low-magnification images indicate the β-W_2N product consists of irregular loosely aggregates of nanoparticles, as shown as Fig. 7a, b. The enlarged SEM image in Fig. 7c suggests

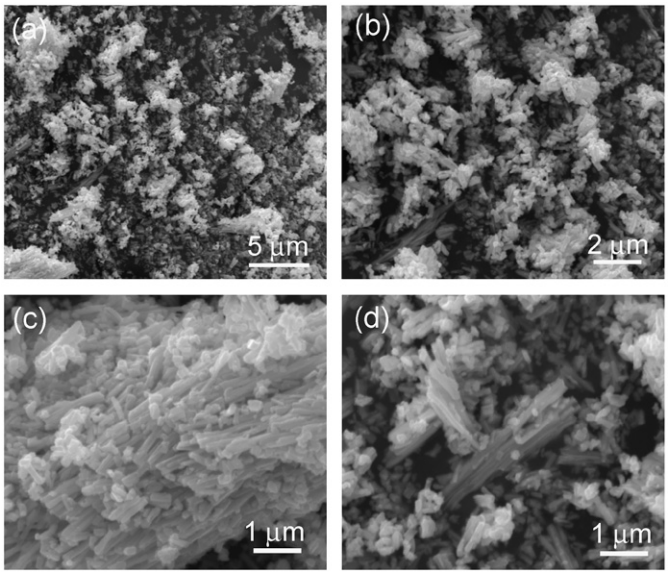

Fig. 7. SEM images with various magnifications of the β-W_2N nanoplates derived from the tungstate-based inorganic–organic hybrid nanobelts.

that the aggregates are apparently composed of "nanorods" with a length-to-diameter ratio range 2–5. Some "nanorods" are bundled together to form a dumpy microrods, as shown in Fig. 7d. One can also find some irregular aggregates that are not rod-like in Fig. 7c, d, and these irregular aggregates may consist of small β-W_2N nanoplates.

Fig. 8 shows the typical TEM observations of the β-W_2N nanocrystals derived from tungstate-based inorganic–organic hybrid nanobelts. Fig. 8a shows a low-magnification TEM image, which indicates the β-W_2N product consists of well-dispersed nanoplates. Most of the nanoplates are of sharp profiles, including triangles, trapezoids and rectangles. The enlarged TEM image shown in Fig. 8b corroborates that the β-W_2N nanoplates obtained are not solid nanorods, but thin nanoplates, according to the shallow contrasts. If they are solid nanorods with diameters of 200 nm, their contrasts in TEM image should be very dark because of the limited penetrating ability of the electrons accelerated by a 200 kV voltage. The contrast from different parts of a nanoplate suggests that some β-W_2N nanoplates are curly or partly scrolled. Fig. 8c shows an individual partly scrolled β-W_2N nanoplate with an apparent dimension of about 200 nm $\times$ 500 nm. The enlarged TEM image in Fig. 8d shows a β-W_2N nanoplate with a dimension of about 130 nm $\times$ 300 nm. Its contrast indicates the nanoplate is composed of nanoparticles with sizes of several nanometers. The corresponding SAED pattern of the β-W_2N nanoplate (Fig. 8d) is shown in Fig. 8e. The SAED pattern consists of a series of concentric diffraction rings superimposed a series of separate diffraction spots, indicating that the β-W_2N nanoplate is composed of small crystalline nanoparticles. The concentric diffraction rings can be readily indexed to the reflections from the cubic β-W_2N phase. The TEM observations are consistent to the XRD results. The grain sizes (about 3.2 nm) of the β-W_2N product calculated from the XRD result are much smaller than the sizes of the plate-like particles from the TEM observations, suggesting that an individual β-W_2N plate-like particle is not a single crystal, but is composed of a great number of small β-W_2N nanocrystals. This point is corroborated by the corresponding SAED pattern with a series of concentric diffraction rings.

When comparing the TEM and SEM images, one may find a disagreement in morphologic determination. The β-W_2N product

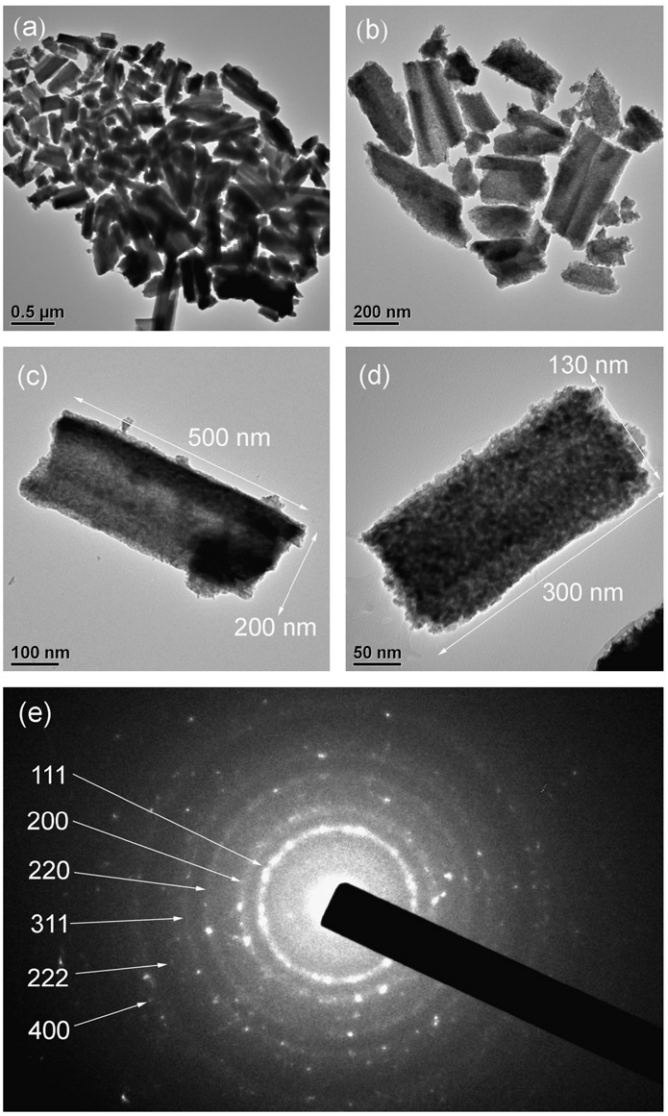

Fig. 8. (a–d) TEM images and (e) SAED pattern of the β-W_2N nanoplates derived from the tungstate-based inorganic–organic hybrid nanobelts.

seems to take on a rod-like morphology judging from the SEM images with low magnifications (Fig. 7), whereas the TEM images show the β-W_2N product consists of polycrystalline plate-like nanocrystals (Fig. 8). The difference in morphologic determination is probably resulted from the difference in SEM and TEM magnifications. The larger rod-like particles should be the aggregates of the smaller β-W_2N nanoplates. In other words, the larger rod-like β-W_2N particles can be separated to smaller β-W_2N nanoplates under a sonication condition.

Fig. 9 shows typical TG-DTA curves of the β-W_2N nanoplates derived from tungstate-based inorganic–organic hybrid nanobelts. The TG curve in Fig. 9a shows that there is a mass loss of 4.8% from room temperature to 350 °C, followed by a sharp mass gain of 8.3% from 350 to 465 °C. There is a small mass loss of 0.4% at 465–800 °C. Fig. 9b shows the corresponding DTA curve. There is a sharp exothermal peak between 400 and 500 °C with a maximum value at 450 °C. In the temperature regions of 100–400 and 500–800 °C, the DTA curve shows weak and broadened exothermal peaks. Considering the TG result together with its corresponding DTA curve, the large mass loss with a sharp exothermal peak at 350–465 °C is mainly due to the oxidation of β-W_2N to WO_3, and the slow mass losses and their

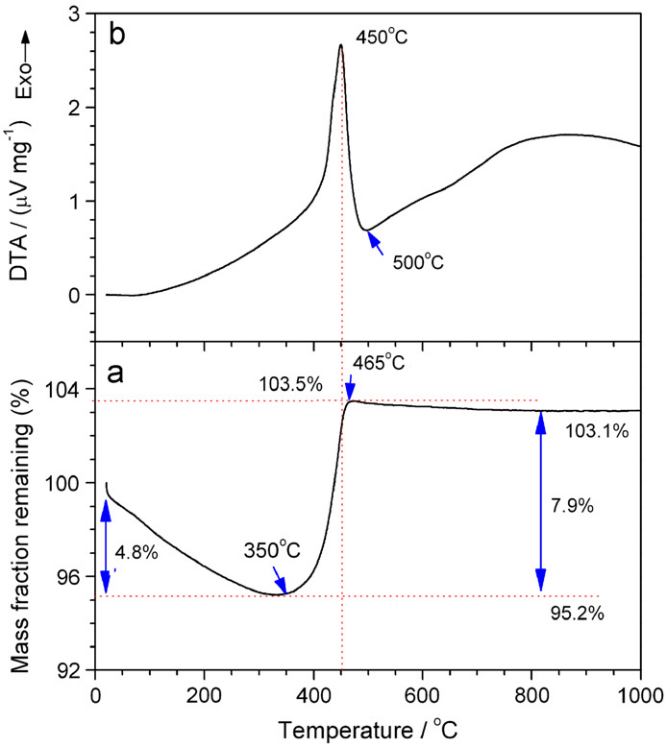

Fig. 9. TG-DTA curves of the β-W_2N nanoplates derived from the tungstate-based inorganic–organic hybrid nanobelts.

corresponding weak exothermal peaks at 100–400 and 500–800 °C should be due to the oxidation of the residual C species. Supposing that β-W_2N and residual C are completely oxidized to be WO_3 and CO_2, respectively, the content of the β-W_2N phase in the sample can be calculated to be 91.7% according to the total mass gain of 3.1% between 100 and 800 °C. It is noted that the oxidation temperature region of the as-obtained β-W_2N nanoplates is 350–500 °C, much less than that of the reported W_2N film (490–640 °C) [29]. The reduced oxidation temperature is probably due to the small grain sizes (about 3.2 nm) for the β-W_2N nanoplates, because the smaller the grain sizes, the higher the oxidizing reaction activity.

Fig. 10 shows a typical FT-IR spectrum of the as-obtained β-W_2N nanoplates. The absorption bands at 3437 and 1630 cm^{-1} correspond to the ν(O–H) stretching and the δ(O–H) bending modes of the adsorbed water molecules, respectively. The peaks at 1401 and around 3132 cm^{-1} are the background absorption bands from KBr. The weak bands at 1000–500 cm^{-1} should belong to the vibration modes of W–N bonds. There are no absorption bands corresponding to organic species, indicating the as-obtained β-W_2N nanoplates do not contain any organic impurities.

4. Discussion

4.1. Formation mechanism of tungstate-based inorganic–organic hybrid nanobelts

H_2WO_4 is a solid acid and *n*-octylamine is an organic base. The acid–base reaction between H_2WO_4 and *n*-octylamine leads to a novel salt of tungstate-based inorganic–organic hybrids. As Figs. 2 and 3 show, the as-obtained tungstate-based inorganic–organic hybrids are of a highly ordered lamellar microstructure and a one-dimensional beltlike morphology. It should be noted that the order degree and morphology of the as-obtained hybrids are strongly

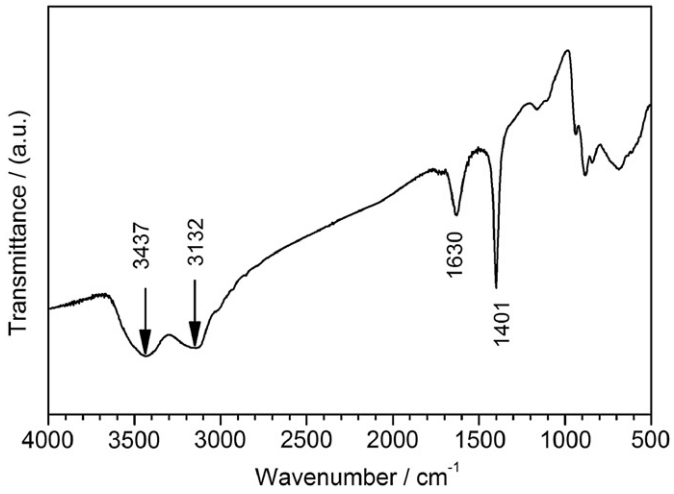

Fig. 10. A typical FT-IR spectrum of the β-W_2N nanoplates derived from the tungstate-based inorganic–organic hybrid nanobelts.

dependent on the reaction conditions, including the water contents and reacting solvent types. In the nonpolar solvent of heptane, the larger the water amounts in the reaction system, the faster the acid–base reaction, the lower the order degree of the hybrid products, and the shorter the length-to-diameter ratios of the one-dimensional structures. When the molar ratio of water to H_2WO_4 is up to 1:2, the product obtained takes on a disclike morphology with apparent diameters of about 1–2 μm. When a polar reagent (i.e., water or ethanol) is used as the reacting solvent, no products with one-dimensional morphology are obtained. These results indicate that the nonpolar solvent plays a key role in the formation of highly ordered one-dimensional tungstate-based inorganic–organic hybrid nanobelts, similar to the case of the reaction of $H_2W_2O_7$ with *n*-alkylamines [38]. In fact, the reaction system of H_2WO_4, *n*-octylamine and heptane is a pseudo water-in-oil microemulsion reactor, which is favorable in formation of the one-dimensional tungstate-based inorganic–organic hybrid nanostructures, not only in the reaction kinetics but also in the morphology control. The related mechanism is close to our previous discussion in the system of $H_2W_2O_7$ and *n*-alkylamines [38].

4.2. Output rate of tungsten nitride

According to Fig. 5, there is a mass loss of 58% when the tungstate-based inorganic–organic hybrid nanobelts are heated from room temperature to 600 °C in an air flow, and the remaining product is WO_3 nanocrystals [43]. The W mass content in the tungstate-based inorganic–organic hybrid nanobelts can be calculated to be 33.3%. If the W atoms in the hybrids are completely transformed to β-W_2N during the NH_3-treatment, the output mass of β-W_2N per 100 g of the hybrids should be about 34 g, i.e., 34%. In the experiment, we can obtain 0.15–0.17 g of product from 0.5 g of the hybrids in the thermal treatment under an NH_3 flow, and therefore the output rate is about 30–34%. The experimental data (30–34%) are very close to the theoretical value (34%), indicating that the product from the tungstate-based inorganic–organic hybrid nanobelts after NH_3-treatment at 750 °C for 2 h is mainly composed of the β-W_2N phase. This analysis can be supported by the XRD and SAED results (Figs. 6a and 8e).

4.3. Formation mechanism of tungsten nitride nanoplates

The formation process of cubic β-W_2N nanoplates from tungstate-based inorganic–organic hybrid nanobelts can be divided

into two steps: (1) forming high active W species from the tungstate-based inorganic–organic hybrid nanobelts, and then (2) nitridizing the as-formed high active W species into β-W_2N nanoplates. The first step is conducted in a non-oxidizing condition at room temperature to 600 °C, and there are at least two basic reactions taking place. One reaction is the removal of structural water from the (WO_6) octahedral frameworks, and the other one is desorption and decomposition of the organic ammonium molecules or ions located in the interlayer spaces of the (WO_6) frameworks. The resultant organic species and the ammonia flow provide a strong reducing atmosphere, in which the inorganic pyrolysates are reduced to WO_y and W, which are of high activity for nitridation. In the second step, the resultant high active species of WO_y and W are nitridized by the NH_3 and newly formed N_2 gases. The decomposition of organic species in the non-oxidizing atmosphere leads to the formation of solid carbon species, but most of the resultant carbon species can be removed by NH_3 at an elevated temperature higher than 600 °C [46]. The possible chemical processes are described as follows:

$$(C_8H_{17}NH_3)_2WO_4 \xrightarrow{\Delta,NH_3} WO_y + W + C \xrightarrow{\Delta,NH_3} \beta\text{-}W_2N \quad (1)$$

The formation of the platelike morphology of the β-W_2N nanocrystals is attributed to the unique precursor of tungstate-based inorganic–organic hybrid nanobelts with a highly ordered lamellar structure. During the course of decomposition and nitridation, the long hybrid belts break into short segments, but their platelike shapes are inherited by the resultant β-W_2N nanocrystals, similar to the topochemical transformation [41]. The as-obtained β-W_2N nanoplates are composed of small β-W_2N nanocrystals with an average crystalline grain size of 3.2 nm, as shown as the XRD and TEM results. In other words, the as-obtained β-W_2N nanoplates are polycrystalline, not single-crystalline, whereas we have used a similar topochemical transformation route to fabricate single-crystalline WO_3 nanoplates from a similar tungstate-based inorganic–organic hybrid precursor [41]. This difference may due to the serious changes in crystal structures during the process from tungstate-based inorganic–organic hybrid belts to β-W_2N nanoplates, when compared with the case from tungstate-based inorganic–organic hybrid belts to WO_3 nanoplates. For the case of WO_3 nanoplates, the crystal structure of the inorganic octahedral (WO_6) layer in the hybrid precursor is similar to that of the resultant WO_3 nanocrystals [41].

We also note that the β-W_2N phase is the only component in the present synthetic condition using gaseous NH_3 as the nitridizing agent. The similar examples can be found in references [34,35,37], where gaseous NH_3 or N_2 are used as the nitridizing agents. However the cases of ammonium dicyanamide [36], and ALD or CVD methods [22–29], other WN_x phases are obtained. This may give us a clue that the state of the nitridizing agents and synthetic processes may account for the difference in the product phases, but further work is needed for deep understanding of the related mechanism.

To demonstrate the necessity of the tungstate-based inorganic–organic hybrid nanobelts for the synthesis of β-W_2N nanoplates, we also synthesized a tungsten nitride sample using commercially available H_2WO_4 powders (Fig. 3d). Fig. 6b shows the XRD pattern of the as-obtained product by nitridizing H_2WO_4 powders in an NH_3 flow. It can also be indexed to be cubic β-W_2N with a calculated cell parameter of $a=0.4171(9)$ nm, which is a little larger than that ($a=0.4133(8)$ nm) of β-W_2N nanoplates. A typical SEM image of the β-W_2N sample derived from H_2WO_4 powders is shown in Fig. 11. One can find that the β-W_2N product from H_2WO_4 powders consists of shape-irregular particles, with a large size distribution (1–5 μm), similar to their precursor of commercial H_2WO_4 powders (Fig. 3d). The above results of comparative experiments corroborate that the plate-like morphology of β-W_2N nanoplates is inherited from the tungstate-based inorganic–organic hybrid nanobelts, which is necessary for the formation of plate-like β-W_2N nanocrystals.

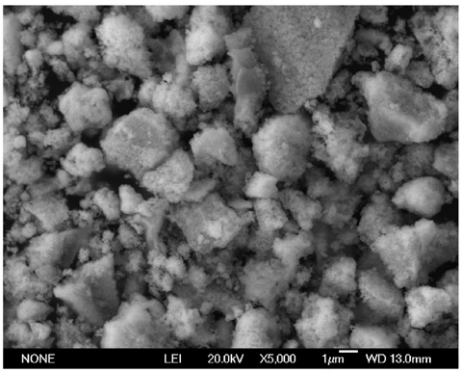

Fig. 11. A typical SEM image of cubic β-W_2N sample derived from commercial H_2WO_4 powders.

5. Conclusions

We have developed an efficient pseudo-morphotactic transformation route to prepare polycrystalline β-W_2N nanoplates via an intermediate product of highly ordered lamellar tungstate-based inorganic–organic hybrid nanobelts as the first example. The tungstate-based hybrid nanobelts were firstly synthesized in a water-in-oil-microemulsion-like reaction system of "commercial H_2WO_4 powders/*n*-octylamine/heptane". The as-obtained hybrid nanobelts were then thermally treated in an ammonia atmosphere at 650–800 °C for 2 h to form cubic β-W_2N nanoplates. The β-W_2N nanoplates consist of small nanocrystals with an average grain size of 3.2 nm. In the thermal treating process, the tungstate hybrid nanobelts are firstly decomposed and reduced to WO_y and W species, which are active and then nitridized to β-W_2N nanocrystals in an ammonia flow. The platelike morphology of the β-W_2N nanocrystals is attributed to the precursor's templating effect of the tungstate-based hybrid nanobelts. The unique polycrystalline structure and platelike morphology make the β-W_2N products obtained have high surface areas and a good dispersibility. The proposed route here is facile and inexpensive, and the as-obtained β-W_2N nanoplates are of promise applications in catalysis and wear-resistant materials.

Acknowledgments

This work was supported by the National Natural Science Foundation of China (Grant no. 50802090), the China Postdoctoral Science Foundation (Grant nos. 20090450094 and 201003397), the Opening Project of the State Key Laboratory of High Performance Ceramics and Superfine Microstructure (Grant no. SKL200905SIC) and the Introduced Talent Project of Zhengzhou University.

References

[1] M. Nagai, H. Nakaya, Mater. Sci. Forum 554 (2007) 65–70.
[2] K.S. Weil, J. Solid State Chem. 177 (2004) 1976–1986.
[3] D. Choi, P.N. Kumta, J. Am. Ceram. Soc. 90 (2007) 3113–3120.
[4] J.C.F. Rodriguez-Reyes, C.Y. Ni, H.P. Bui, T.P. Beebe, A.V. Teplyakov, Chem. Mater. 21 (2009) 5163–5169.
[5] H.X. Zhong, X.B. Chen, H.M. Zhang, M.R. Wang, S.S. Mao, H.X. Zhong, X.B. Chen, H.M. Zhang, M.R. Wang, S.S. Mao., Appl. Phys. Lett. 91 (2007) 163103.

[6] L.-T. Fu, Z.-G. Chen, D.-W. Wang, L. Cheng, H.-Y. Xu, J.-Z. Liu, H.-T. Cong, G.Q. Lu, J. Zou, J. Phys. Chem. C 114 (2010) 9627–9633.
[7] G. Liu, J.O. Li, K. Chen, H. Zhou, C. Pereira, J. Ferreira, Cryst. Growth Des. 9 (2009) 562–568.
[8] Y. Ma, Q. Cui, L. Shen, Z. He, J. Appl. Phys. 102 (2007) 013525.
[9] V. Chakrapani, J. Thangala, M.K. Sunkara., Int. J. Hydrogen Energy 34 (2009) 9050–9059.
[10] T. Polcar, N.M.G. Parreira, A. Cavaleiro., Wear 265 (2008) 319–326.
[11] H.M. Ajmera, T.J. Anderson, J. Koller, L. McElwee-White, D.P. Norton, Thin Solid Films 517 (2009) 6038–6045.
[12] Z. Wang, Z. Liu, Z. Yang, S. Shingubara, Microelectron. Eng. (2008) 395–400.
[13] Z.W. Li, R.G. Gordon, D.B. Farmer, Y.B. Lin, J. Vlassak, Electrochem. Solid State 8 (2005) G182–G185.
[14] P.C. Jiang, Y.S. Lai, J.S. Chen, J. Electrochem. Soc. 153 (2006) G572–G577.
[15] C.Y. Lu, E.Y. Chang, J.C. Huang, C.T. Chang, M.H. Lin, C.T. Lee, J. Electron. Mater. 37 (2008) 624–627.
[16] S.H. Kim, J.K. Kim, J.H. Lee, N. Kwak, J. Kim, S.H. Jung, M.R. Hong, S.H. Lee, J. Collins, H. Sohn., J. Electrochem. Soc. 154 (2007) D435–D441.
[17] V. Miikkulainen, M. Suvanto, T.A. Pakkanen, S. Siitonen, P. Karvinen, M. Kuittinen, H. Kisonen, Surf. Coat. Technol. 202 (2008) 5103–5109.
[18] H. Tominaga, M. Nagai, Electrochim. Acta 54 (2009) 6732–6739.
[19] Z.W. Yao, H.T. Dong, Appl. Surf. Sci. 255 (2008) 2259–2264.
[20] D.V. Suetin, I.R. Shein, A.L. Ivanovskii, J. Struct. Chem. 51 (2010) 199–203.
[21] B.H. Yu, C.L. Wang, X.Y. Song, Q.J. Sun, D. Chen, J. Alloys Compd. 487 (2009) 556–559.
[22] A.M. Hoyas, J. Schuhmacher, C.M. Whelan, T. Fernandez Landaluce, D. Vanhaeren, K. Maex, J.P. Celis, J. Appl. Phys. 100 (2006) 114903.
[23] A.M. Hoyas, Y. Travaly, J. Schuhmacher, T. Sajavaara, C.M. Whelan, B. Eyckens, O. Richard, S. Giangrandi, B. Brijs, W. Vandervorst, K. Maex, J.P. Celis, A.M. Jonas, A. Vantomme, J. Appl. Phys. 99 (2006) 063515.
[24] A.B. Mukhopadhyay, C.B. Musgrave, Appl. Phys. Lett. 90 (2007) 173120.
[25] C.L. Dezelah, O.M. El-Kadri, K. Kukl, K. Arstila, R.J. Baird, J. Lu, L. Niinisto, C.H. Winter, J. Mater. Chem. 17 (2007) 1109–1116.
[26] Y.S. Won, Y.S. Kim, T.J. Anderson, L.L. Reitfort, I. Ghiviriga, L. McElwee-White, J. Am. Chem. Soc. 128 (2006) 13781–13788.
[27] Y.W. Yang, J.B. Wu, J.L. Wang, Y.F. Lin, H.T. Chiu, Surf. Sci. 600 (2006) 743–754.
[28] S.D. Kim, Curr. Appl. Phys. 7 (2007) 426–433.
[29] S.H. Mohamed, Surf. Coat. Technol. 202 (2008) 2169–2175.
[30] P. Hones, N. Martin, M. Regula, F. Levy, J. Phys. D: Appl. Phys. 36 (2003) 1023–1029.
[31] Y.Z. Tsai, J.G. Duh, Surf. Coat. Technol. 201 (2006) 4266–4272.
[32] K.S. Weil, J.Y. Kim, P.N. Kumta, Mater. Lett. 39 (1999) 292–297.
[33] A. Rugge, J.S. Becker, R.G. Gordon, S.H. Tolbert, Nano Lett. 3 (2003) 1293–1297.
[34] C.L. Dezelah, O.M. El-Kadri, M.J. Heeg, C.H. Winter, J. Mater. Chem. 14 (2004) 3167–3176.
[35] A. Rugge, J.S. Becker, R.G. Gordon, S.H. Tolbert, Nano Lett. 3 (2003) 1293–1297.
[36] M. Lei, H.Z. Zhao, H. Yang, B. Song, P.G. Li, W.H. Tang, Mater. Lett. 62 (2008) 1539–1542.
[37] P. Bai, W. Xing, Z.F. Yan, J. Porous Mater. 13 (2006) 173–180.
[38] D. Chen, Y. Sugahara, Chem. Mater. 19 (2007) 1808–1815.
[39] D. Chen, Y. Sugahara, Key Eng. Mater. 352 (2007) 85–88.
[40] D. Chen, H. Wang, R. Zhang, S. Guan, H.X. Lu, H. Xu, D. Yang, Y. Sugahara, L. Gao, Chem. J. Chin. Univ. 29 (2008) 1325–1330.
[41] D. Chen, L. Gao, A. Yasumori, K. Kuroda, Y. Sugahara, Small 4 (2008) 1813–1822.
[42] D. Chen, H. Wang, R. Zhang, L. Gao, Y. Sugahara, J. Ceram. Process. Res. 9 (2008) 596–600.
[43] D. Chen, H. Wen, H. Chen, H. Wang, R. Zhang, H. Xu, D. Yang, H. Lu, Mater. Chem. Phys. 116 (2009) 507–513.
[44] D. Chen, X. Hou, H. Wen, Y. Wang, H. Wang, X. Li, R. Zhang, H. Lu, H. Xu, S. Guan, J. Sun, L. Gao, Nanotechnology 21 (2010) 035501.
[45] B. Ingham, S.V. Chong, J.L. Tallon, J. Phys. Chem. B 109 (2005) 4936–4940.
[46] P.G. Li, M. Lei, W.H. Tang, Mater. Res. Bull. 43 (2008) 3621–3626.